

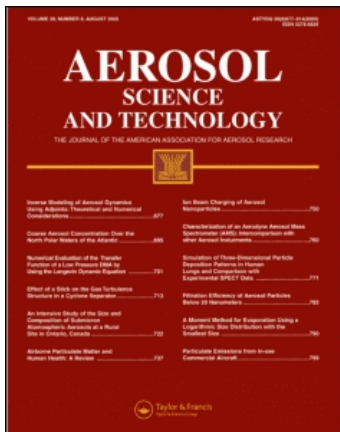
This article was downloaded by: [University of Washington Libraries]

On: 16 December 2009

Access details: Access Details: [subscription number 907134054]

Publisher Taylor & Francis

Informa Ltd Registered in England and Wales Registered Number: 1072954 Registered office: Mortimer House, 37-41 Mortimer Street, London W1T 3JH, UK



Aerosol Science and Technology

Publication details, including instructions for authors and subscription information:

<http://www.informaworld.com/smpp/title~content=t713656376>

Size-Dependent Collection Efficiency of an Airborne Counter flow Virtual Impactor

Mary L. Laucks^a; Cynthia H. Twohy^b

^a DEPARTMENT OF ATMOSPHERIC SCIENCES, UNIVERSITY OF WASHINGTON, SEATTLE, WA ^b NATIONAL CENTER FOR ATMOSPHERIC RESEARCH, BOULDER, CO

First published on: 01 January 1998

To cite this Article Laucks, Mary L. and Twohy, Cynthia H.(1998) 'Size-Dependent Collection Efficiency of an Airborne Counter flow Virtual Impactor', *Aerosol Science and Technology*, 28: 1, 40 – 61, First published on: 01 January 1998 (iFirst)

To link to this Article: DOI: 10.1080/02786829808965511

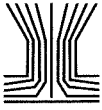
URL: <http://dx.doi.org/10.1080/02786829808965511>

PLEASE SCROLL DOWN FOR ARTICLE

Full terms and conditions of use: <http://www.informaworld.com/terms-and-conditions-of-access.pdf>

This article may be used for research, teaching and private study purposes. Any substantial or systematic reproduction, re-distribution, re-selling, loan or sub-licensing, systematic supply or distribution in any form to anyone is expressly forbidden.

The publisher does not give any warranty express or implied or make any representation that the contents will be complete or accurate or up to date. The accuracy of any instructions, formulae and drug doses should be independently verified with primary sources. The publisher shall not be liable for any loss, actions, claims, proceedings, demand or costs or damages whatsoever or howsoever caused arising directly or indirectly in connection with or arising out of the use of this material.



Size-Dependent Collection Efficiency of an Airborne Counterflow Virtual Impactor

Mary L. Laucks*

DEPARTMENT OF ATMOSPHERIC SCIENCES, BOX 351640, UNIVERSITY OF WASHINGTON,
SEATTLE, WA 98195

Cynthia H. Twohy

NATIONAL CENTER FOR ATMOSPHERIC RESEARCH, P.O. BOX 3000, BOULDER, CO 80307-3000

ABSTRACT. A three-dimensional numerical model of an airborne counterflow virtual impactor (CVI) was made, and its steady state airflow velocity field was calculated using a commercially available fluid dynamics code (STAR-CD). Size-dependent impaction and front-end (first 0.2 m) collection efficiencies were determined from the analysis of non-evaporating droplet trajectories calculated from the velocity solutions, assuming the droplets stick upon impaction with inlet surfaces. The general features of the velocity field solutions agree well with a two-dimensional model with idealized geometry. Models were made for two values of counterflow, 1.0 lmin^{-1} and 3.0 lmin^{-1} , in order to investigate different cut sizes. The locations of the stagnation planes in both models agreed with those calculated from simple geometrical considerations. The impaction efficiency curves show cut sizes of $10.1 \mu\text{m}$ and $17.0 \mu\text{m}$ for 1 lmin^{-1} and 3 lmin^{-1} counterflows, respectively. Calculated collection efficiencies are in general agreement with results from CVI field measurements. AEROSOL SCIENCE AND TECHNOLOGY 28:40–61 (1998) © 1998 American Association for Aerosol Research

INTRODUCTION

The counterflow virtual impactor (CVI) is an instrument technology developed jointly at the Universities of Washington and Stockholm and is presently used for airborne cloud sampling at the University of Stockholm and the National Center for Atmospheric Research (NCAR). The CVI was designed to separate cloud elements (droplets or ice crystals) of different sizes from the interstitial particles and gases in a cloud. Cloud elements impact on a counterflow of

heated carrier gas as they enter the tip region, and those larger than a certain aerodynamic diameter (the diameter that would make the particle aerodynamically equivalent to a unit density sphere) have enough inertia to pass through the counterflow region and be collected by the CVI (Fig. 1). Because of their relatively large size and high inertia, cloud elements can readily cross flow streamlines. The condensed water in these large particles is evaporated rapidly but at a rate slow compared with the impaction time, leaving residual particles, water vapor, and other volatile components in the sample airstream. The physical and chemical

*Current Address: Department of Chemical Engineering, Box 351750, University of Washington, Seattle, Wa. 98195.

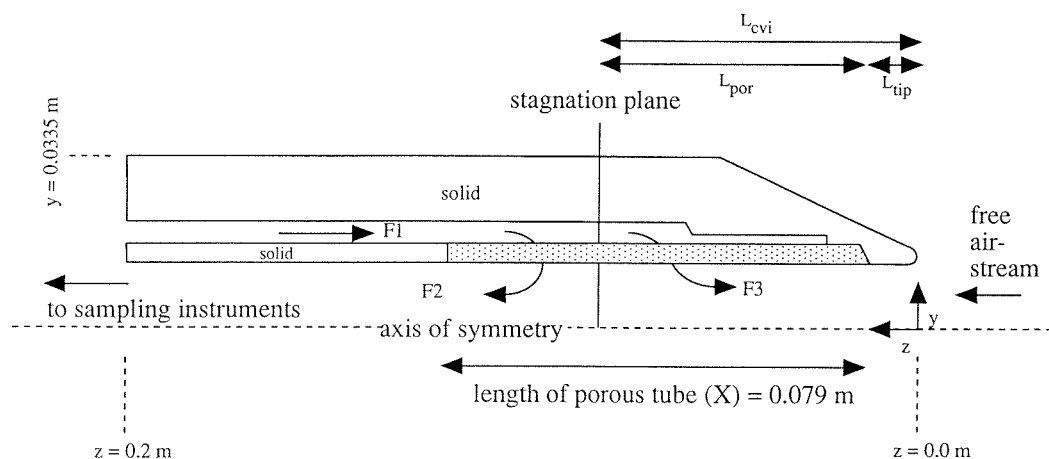


FIGURE 1. Schematic of one quarter of the CVI inlet front end. The free airstream due to the forward motion of the aircraft is along the axis of the CVI. The flows F2 and F3 separate forming a stagnation plane where the velocity of the flow field is nearly zero. $F1 = F2 + F3$. The distance from the CVI tip to the stagnation plane is L_{cvi} , and is the sum of L_{por} + L_{tip} . The CVI front end is 0.2 m in length and 0.0335 m in diameter.

properties of the residual particles and volatile gases then can be measured or analyzed by sensors downstream of the CVI inlet. The location of the “stagnation” plane, where the velocity of the air along the axis is zero, and the size of the droplets collected are determined by the length of the porous tube, the ratio of the counterflow to the main flow through the outer wall of the CVI, and the details of the flow field in the tip region (Fig. 1).

Originally flown in Europe on a Falcon-20 jet (Ogren et al., 1985), the CVI has been used in ground-based and airborne studies for about ten years. The CVI has provided useful information regarding the chemical and physical properties of liquid cloud droplets in both marine and continental clouds (Noone et al., 1988a; Ogren et al., 1989; Twohy et al., 1989; Noone et al., 1991; Ogren et al., 1992). One of the most exciting new applications of the CVI has been to measure cirrus cloud condensed water content and number concentration (Noone et al., 1993; Strom et al., 1994), properties critically important to global climate, yet not well characterized.

The CVI inlet modeled here has been flown on the NCAR Electra aircraft, where

it is mounted on the aircraft fuselage with the inlet tip well outside the aircraft boundary layer. Potential-flow modeling of the airflow around the aircraft (Twohy and Rogers, 1993) is used to determine the mean flow angle at the inlet mounting location, and the inlet is aligned accordingly. With turbulence or changes in aircraft flight attitude, however, the actual airflow angle impinging on the CVI probe can deviate by up to a few degrees. A shroud has been developed to straighten airflow into the CVI (Twohy et al., 1997), so the airflow is assumed to be isoaxial in the models discussed below. The CVI model is oriented such that in a Cartesian coordinate system the \hat{z} axis runs along the axis of the CVI in the direction of the free airstream relative velocity (opposite to the direction of the aircraft motion).

Figure 1 is a cross-section (in the \hat{y} - \hat{z} plane) of one quarter of the CVI showing schematically how a flow of heated carrier gas (filtered, dry air, or nitrogen), $F1$, is pumped through an annular region and moves radially inward through a porous tube at the tip of the CVI inlet. The flow then separates; most of it comprises the sample flow, $F2$, which is drawn in the $+\hat{z}$ direction (axially) to various sensors, but the remain-

ing gas is forced out the probe tip as the counterflow, $F3$ in the $-\hat{z}$ direction. The counterflow efficiently prevents small interstitial particles and gases from entering the probe tip. Larger cloud elements have sufficient inertia to deviate from the flow streamlines that diverge around the probe tip and enter the slowly moving counterflow airstream. The stagnation plane is located a distance L_{cvi} from the CVI tip. The length of the tip region is denoted L_{tip} and the length from the tip end of the porous tube to the stagnation plane is denoted L_{por} .

$$L_{por} + L_{tip} = L_{cvi}$$

Previously, impaction efficiency curves for different CVI designs have been determined experimentally by using droplets of ammonium sulfate solution at high relative humidities (Noone et al., 1988b) and dry glass beads (Anderson et al., 1993). From these experimental curves, cut sizes (the droplet diameter that is collected with 50% efficiency) and

cut sharpness ($= \sqrt{\frac{D_{84}}{D_{16}}}$, where D_{84} and

D_{16} are the diameters at 84% and 16% impaction efficiency, respectively) can be estimated. Typically, the accuracy of empirical efficiency curves is limited by experimental difficulties in generating, transporting, and counting the calibration particles. Anderson's results (Anderson et al., 1993) with dry glass beads show a higher cut sharpness than wet calibration methods, but the efficiency curves show a falloff over a range of 2–3 μm around the cut sizes.

Cut size also can be estimated theoretically from aerodynamic drag theory. However, this theory is based on approximations for the behavior of the counterflow and tip flow field. Therefore, previous experimental and theoretical estimations of cut size for a CVI have been limited in resolution and accuracy. Furthermore, compilation of CVI data from various experiments (Twohy, 1992; as well as unpublished data) suggests that subsequent to entering the CVI tip, cloud elements may be transmitted with less than 100% efficiency.

More recently, a numerical two-dimen-

sional CVI model was constructed, and flow solutions were obtained using the equations for two-dimensional cylindrical steady-state potential flow (Lin and Heintzenberg, 1995). The geometry of this model was quite simple compared with that of the actual CVI probe. The probe was modeled as a very thin wall (0.0001 m) with an outflow boundary condition representing the flow $F1$ through the porous tube with a length of 0.017 m. The model was used to calculate droplet trajectories and determine cut sizes for different flow regimes. The cut sizes (taken to be the diameter at which the efficiency is 50%) agree with those in a previous experimental study (Anderson et al., 1993), but the model predicts a much higher cut sharpness than is observed experimentally.

The recent acquisition of a commercial computational fluid dynamics code (STAR-CD)¹ made possible the numerical calculation of a flow field for the CVI using the full three-dimensional Navier-Stokes equations and a model for atmospheric turbulence. Because this code includes pre-processing software that simplifies the process of defining the geometry of the models, it was possible to model the exact geometry of the CVI probe with some simplifications where symmetry existed. Trajectories of different-sized droplets were calculated based on the detailed three-dimensional flow-field solution. Impaction efficiency curves were determined from these trajectory calculations, and cut sizes were obtained for different counterflow configurations. With this method, cut sizes were calculated directly from a calculated velocity solution, without making assumptions about the form or effects of the velocity field. Although the models discussed below do not include evaporating droplets, the code has the capability of including heat and mass transfer between the droplets and the air. Therefore, in future work we could accurately predict the transport efficiency of

¹ STAR-CD was developed by Computational Dynamics Limited, Olympic House, 317 Latimer Road, London W10 6RA and is distributed by Adapco, 60 Broadhollow Rd., Melville, N. Y. 11747, (516) 549-2300.

the evaporating droplets as they travel through the CVI inlet stagnation plane.

Our primary goals in the present research were (1) to further refine the accuracy of previous cut size and impaction efficiency calculations, (2) to determine the most likely causes of imperfect transport efficiency once droplets have passed the stagnation plane, and (3) to develop a framework of models for future calculations of transport efficiency in order to design better inlets for upcoming experiments.

THE COMPUTATIONAL MODEL FOR THE CVI

The three-dimensional computational mesh for the model consisted of the straight front end of the CVI inlet. The 90° bend that connects the front end of the CVI to the inside of the aircraft and the sampling instruments was not included in this model. Because the CVI is axisymmetric, only half of the CVI was modeled. Figure 2b shows

the geometry of the CVI tip broken into hexagonal and prism cells and indicates the location and type of boundary conditions. Table 1 summarizes the CVI characteristics.

Geometry of the CVI

The model for the front end of the CVI inlet duplicates the actual details of the CVI flown previously on the NCAR Electra. A hollow inner tube with a radius of 0.0031 m is enclosed by a thin porous annulus of thickness equal to 0.0015 m. An annular space between the porous tube and the outer wall of the CVI provides the supply of air that flows through the porous tube. The porous tube is 0.079 m long and starts 0.0017 m downstream of the CVI tip. The foremost edge of the CVI tip is slightly rounded to reduce turbulence. The outside radius of the CVI is 0.0335 m and the front end has a length of 0.20 m. The inner radius of the CVI increases toward the pump end in

TABLE 1. Summary of CVI Characteristics

Free airstream velocity		110 m/s
Tip geometry		rounded
Inner radius (tip)		0.0031 m
Porous tube length		0.0791 m
Effective length		0.0762 m
Ambient pressure		900 mb
Ambient temperature		20°C
CVI temperature		50°C
A) Counterflow = 1 lmin⁻¹		
F3		1.0 lmin ⁻¹
F1		9.5 lmin ⁻¹
F2		8.5 lmin ⁻¹
Stagnation plane location	from CFD	0.0123 m
	from simple theory $\left(L_{cvi} = \frac{F3}{F1} X\right)$	0.0100–0.0126 m
Cut size	from CFD	10.1 μm
	from stop dist. theory	9.25–12.3 μm
Stop distance of cut size		$L_{cvi} + 0.3 R$
B) Counterflow = 3 lmin⁻¹		
F3		3.0 lmin ⁻¹
F1		9.5 lmin ⁻¹
F2		6.5 lmin ⁻¹
Stagnation plane location	from CFD	0.0285 m
	from simple theory	0.0267–0.0340 m
Cut size	from CFD	17.0 μm
	from stop dist. theory	15.4–16.9 μm
Stop distance of cut size		$L_{cvi} + 0.9 R$

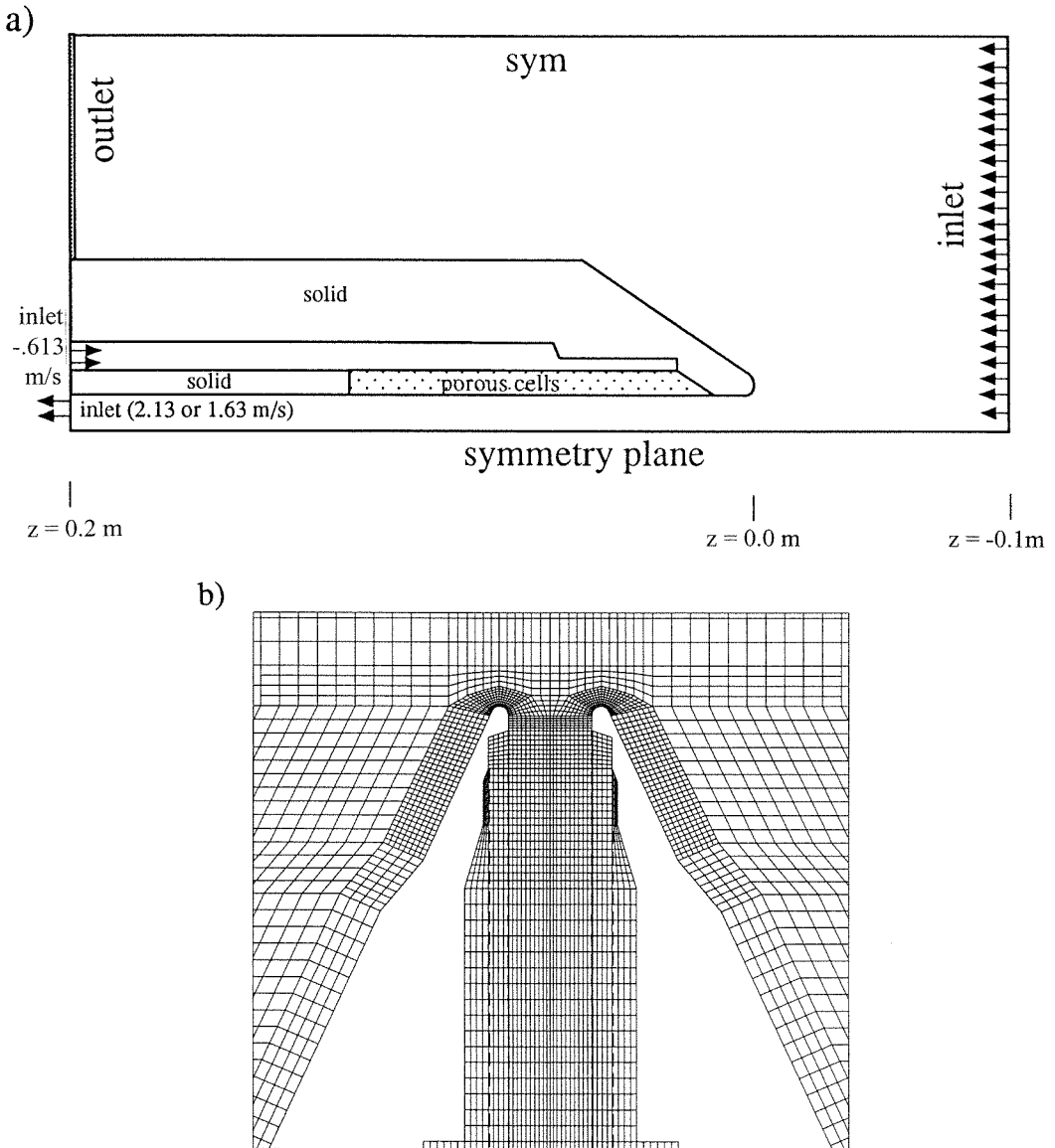


FIGURE 2. Boundary conditions and tip mesh for numerical model. (a) Three inlet boundary conditions (velocity specified), an outlet condition (velocity direction, but not magnitude specified), and a symmetry condition are placed on the model as indicated. In addition the porous tube is modeled as a distributed resistance. All other boundaries are solid walls. (b) Mesh cross-section showing more refined cells near CVI tip.

stages until it joins a 90° bend, which is not included in this model. At this point, the inner radius of the CVI is 0.0046 m.

The ambient air around the outside of the CVI inlet was modeled as an annular region

extending from the outer walls of the CVI ($r = 0.035$ m) to $r = 0.15$ m. The model contained roughly 149,000 hexahedral cells of varying sizes, with smaller cells in areas of high curvature, where more detail was required.

Boundary Conditions

Three types of boundary regions were defined for the model (Fig. 2): regions where the velocity was defined ("inlets"), regions where outflow but not the velocity magnitude was specified ("outlets"), and regions of symmetry ("sym"). Figure 2a shows the location of the different boundary conditions. The airstream velocity (110 m/s in the $+\hat{z}$ direction) was imposed at a plane 0.10 m upstream of the CVI tip. The velocities corresponding to the volumetric flow rates $F1$ and $F2$ were set on the annular ($0.0064 < r < 0.011$ m) and circular regions ($r < 0.0046$ m) at the downstream end of the CVI front end ($z = 0.2$ m). An outlet condition was defined on the $z = 0.2$ m plane for $r > 0.035$ m. On the outer walls of the model space (at $r = 0.15$ m), symmetry boundary conditions were imposed, allowing the flow field to appear infinite in extent. The symmetry boundary condition also was placed on the symmetry plane, which allowed the half-CVI to appear physically like a whole CVI. Wall boundary conditions (i.e. $u, v, w = 0$ m/s) were imposed at all solid surfaces of the model.

The two flow models of the CVI front end were identical except for the velocity imposed in the region $r < 0.0046$ m at the $z = 0.2$ m plane. The velocities were 2.13 m/s and 1.63 m/s in the $+\hat{z}$ direction, for flows of 8.5 lmin^{-1} and 6.5 lmin^{-1} , respectively. This corresponds to actual flow variations imposed during flight to change the counterflow rate and therefore the droplet cut size. The velocity in the region $0.0064 < r < 0.011$ m at $z = 0.2$ m corresponding to the flow toward the tip through the outer annulus was 0.613 m/s (9.5 lmin^{-1}) in the $-\hat{z}$ direction in both cases.

Porosity

The porous tube in the CVI was manufactured by Newmet Krebsoge, Inc. by a process of cold isostatic pressing of powdered stainless steel and subsequent sintering that gives the material stability and uniformity, approximately $20 \mu\text{m}$, pore size. The porous

tube was modeled as a distributed resistance to flow that defines the permeability coefficients α and β in the equation

$$\frac{\partial P}{\partial x} = -(\alpha_x u_x^2 + \beta_x u_x).$$

where x is either $r, \phi,$ or z . The permeability coefficients as supplied by the manufacturer are

$$\alpha_r = \alpha_\phi = \alpha_z = 5.48 \times 10^5 \frac{\text{kg}}{\text{m}^4}$$

$$\beta_r = \beta_\phi = \beta_z = 3.02 \times 10^6 \frac{\text{kg}}{\text{m}^3 \text{s}}.$$

The porosity also was modeled with the same coefficients in the radial direction but with effectively infinite (10^4 times larger) values in the z and ϕ directions, which would correspond to an infinite pressure drop (or no flow) in the z and ϕ directions. In this case the location of the stagnation plane was observed to move about 7% farther away from the tip. This is because a solid region abuts the end of the porous tube between $z = 0.0017$ m and $z = 0.0046$ m, restricting entry of air flow in the $+\hat{r}$ direction. When no flow is permitted to enter through the porous tube in the \hat{z} direction either, this portion of the tube is effectively a solid surface, and the entire flow pattern is shifted downstream of the tip. In the models discussed below, the permeability was isotropic, as shown in the above equations.

Control Parameters

For both models, the airflow was assumed to be steady-state, so that the time-independent Navier-Stokes equations could be used. These equations are solved on each cell of the model by the finite volume method (Patankar, 1980). The convective and diffusive terms in the Navier-Stokes equations are approximated by linearizations of nearest neighbor values, and the convergence algorithm used is called the Semi-Implicit Method for Pressure Linked Equations (SIMPLE) (Patankar and Spalding, 1972). For completeness, air was assumed to be

compressible since there is at least a 5% density increase at the Mach number of the aircraft (0.3). However, an assumption of incompressible flow, such as used by Lin and Heintzenberg (1995), may be sufficient inside the CVI.

Turbulence

The turbulence model used to simulate atmospheric turbulence was the renormalization group (RNG) k - ϵ model, where k is the turbulent kinetic energy and ϵ is the turbulent kinetic energy dissipation rate. The model solves two differential equations, one for k and one for ϵ and is appropriate for flows near walls, as well as for free shear flows. The RNG k - ϵ model is a variation on the standard k - ϵ model (Launder and Spalding, 1974) and has been shown to successfully predict flows with recirculation (Yakhot et al., 1992). We therefore consider it appropriate for the CVI flow field, which contains regions of high curvature.

The turbulence model parameters were chosen based on consideration of both measured turbulence intensities (TI) and the ratio of turbulent viscosity to laminar viscosity as calculated by the model. The turbulent viscosity is related to TI and a turbulence length scale, TL , by the relation, $\mu_t = \sqrt{3/2} \rho f_\mu C_\mu^{1/4} TI TL U$, where f_μ and C_μ are constants and U is the local velocity magnitude. For most model runs, the turbulence intensity was assumed to be 5% of the free airstream velocity, and the turbulent to laminar viscosity ratio was adjusted (by changing TL) to be in the range of 100–200, which is considered moderate turbulence (Adapco, private communication). Turbulence parameters are imposed as boundary conditions at the upstream inlet boundary of the model. The turbulence model then calculates the velocity field including the effects of turbulence propagated throughout the model. Particle trajectories are determined by the velocity at the centroid of each mesh cell, and so are influenced indirectly by turbulence. However, the particle trajectories did not interact stochastically with the turbulent eddies.

Actual turbulence levels encountered during sampling with the CVI will vary depending on cloud type and altitude. To address the sensitivity of the solution to turbulence parameters, model runs were also made for $TI = 0.5\%$ and a turbulent to laminar viscosity ratio of approximately 100, and another run was made with $TI = 5\%$ and a turbulent to laminar viscosity ratio of about 3000. The stagnation plane location was not sensitive to either change, but the cut size decreased by $1 \mu\text{m}$ for the $TI = 0.5\%$ run, and increased by $1 \mu\text{m}$ for $TI = 5\%$ and viscosity ratio of 3000.

VELOCITY SOLUTIONS FOR CVI MODEL

Figure 3 is an illustration of the complete velocity solution for the flow around the outside of the CVI. The velocity vectors have been plotted using a uniform grid (not the actual mesh) for ease of presentation. The lengths of the vectors are scaled proportionally to the velocity magnitudes so that flow inside the CVI (with magnitudes only a fraction of those in the free airstream) cannot be seen. The centerline airflow slows as it approaches the essentially stagnant air within the CVI tip but is accelerated as it is diverted around the outside of the CVI inlet. The location upstream of the CVI tip where the streamlines first begin to diverge from axial flow was found to be a strong function of axial location and ranged from about 0.4 to 1.6 inlet (inner) diameters upstream of the CVI tip for the streamlines near the centerline and for those near the walls, respectively.

Figures 4a and 4b show details of the velocity solutions obtained for the two flow configuration models of the CVI (model A: counterflow = 1 lmin^{-1} and model B: counterflow = 3 lmin^{-1}). Both figures show just the tip end of the CVI, and the vector lengths are fixed at a constant length regardless of magnitude so that the small velocities inside the tip are visible and their directions apparent. Flow outside the aircraft (moving at $\sim 110 \text{ m/s}$) impinges axially on the tip of the CVI, but the counterflow airstream prevents the outside air from entering the CVI.

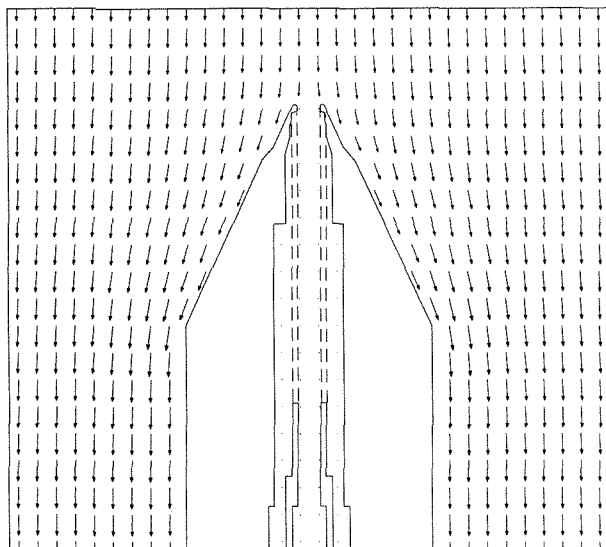


FIGURE 3. Velocity field for CVI. Outside the CVI, air accelerates as it flows around the edge of the CVI. The length of the velocity vectors are proportional to the velocity magnitude, so that velocity magnitudes inside the CVI are too small to be seen.

The overall flow fields are similar, both having two regions, S_1 and S_2 , where the velocity is approximately zero in the z direction (stagnation planes): S_1 is just inside the tip where the free airstream meets the counterflow, and S_2 is farther downstream where the sample airstream (F_2) separates from the counterflow (F_3). S_2 is much farther away from the tip for a larger counterflow (3 l min^{-1}) while S_1 is slightly closer to the tip. S_1 moves closer to the tip because for the same free airstream velocity a larger counterflow velocity will push the separation region farther out the tip. The location of the second stagnation plane varies with counterflow rate, as is expected from simple calculations and previous experiments.

These results agree qualitatively with those from the Lin and Heintzenberg (1995) model. In that model different counterflow velocities were used, but the qualitative behavior of the stagnation planes was the same; that is, S_1 moved slightly toward the tip for larger counterflow velocity, while S_2 moved away from the tip. In the Lin and Heintzenberg model, as in this study, S_1 was found to be curved, in contrast to S_2 .

The calculation of the velocity fields proceeded until the sum of the residuals for the three components of momentum, pressure,

and mass flux over all the cells in the model were no greater than 10^{-6} . One indication of whether the calculations have converged sufficiently is how closely the mass flux of air, using the calculated field velocity, approximates the mass flux calculated from the imposed boundary condition values, or, in the case of the counterflow from the tip, the expected flow difference ($F_1 - F_2$). The mass flux (kg/sec) through an area A is equal to $\sum_i v_i \rho_i$, where i runs over all the cell faces on A , ρ_i is the density of air in the i th cell, and v_i is the velocity of the air on the i th cell face.

For model A, checks of the mass flux through the tip, the porous tube, and the two downstream "inlets" (Fig. 2a) show that the discrepancies between the fluxes as calculated by the model versus that expected by design are all less than 0.5%. For model B, checks of the mass flux through the various boundaries show that the discrepancies are less than 0.4%. For both flow configurations, the mass flux checks verify that the models are well converged.

The stagnation plane for model A is found to be at $z = 0.0123 \text{ m}$. This agrees well with the simple geometrical calculation ($L_{por} = (F_3/F_1)X$), which predicts a stagnation plane location, (L_{cvi}), between $z = 0.0100$

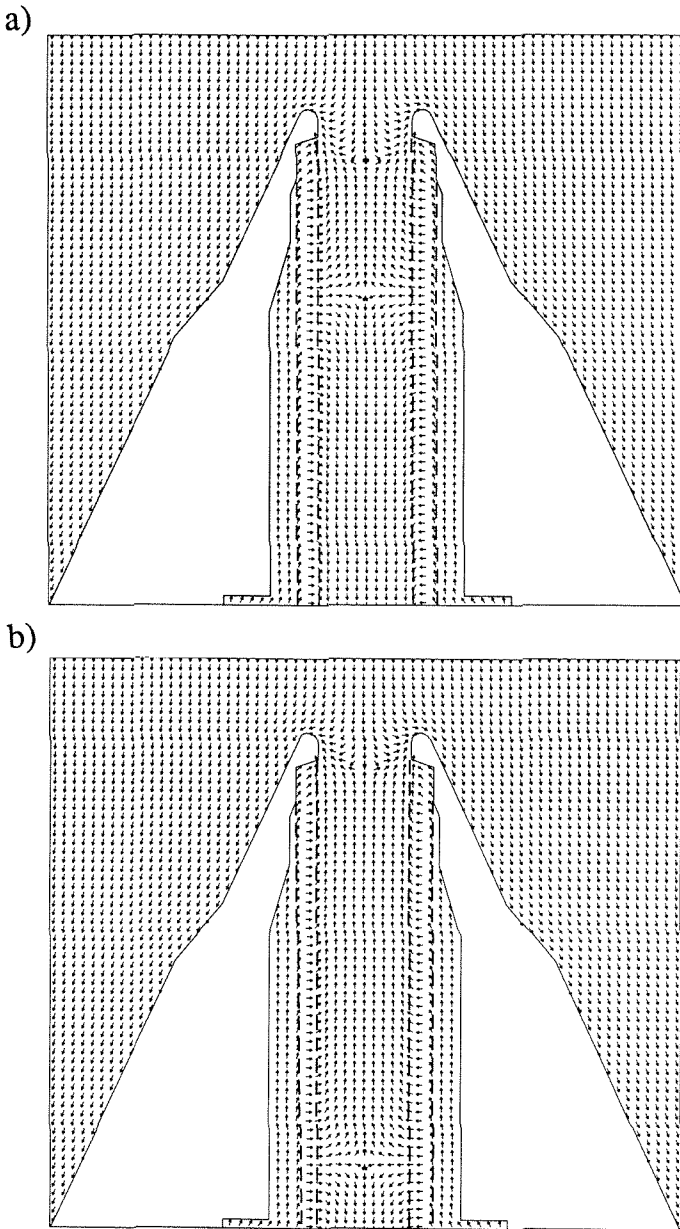


FIGURE 4. Tip region of velocity solution: (a) $F_3 = 1.0 \text{ lmin}^{-1}$, (b) $F_3 = 3.0 \text{ lmin}^{-1}$. Two stagnation planes are visible on both plots: S_1 defines the separation between the free airstream and the counterflow, and S_2 defines the separation between the counterflow and the sample airstream. S_1 is curved and its location is relatively insensitive to counterflow rate.

m and $z = 0.0126 \text{ m}$, depending on whether the porous tube length, X , is taken to be the full physical length (i.e., $z = 0.0017$ to $z =$

0.0808 m), or only the length of the portion that is not abutting against a solid region (i.e., $z = 0.0046$ to $z = 0.0808 \text{ m}$). The

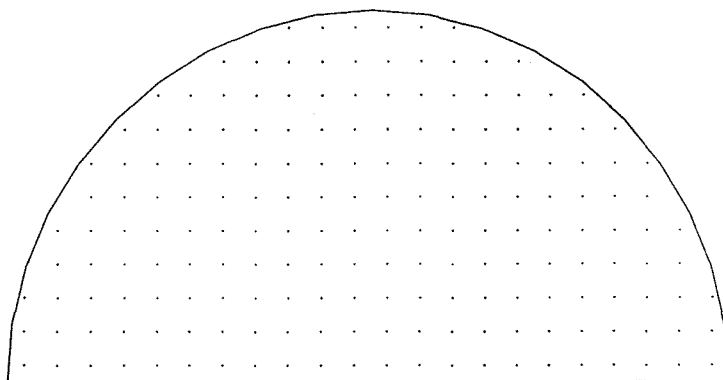


FIGURE 5. Initial droplet positions relative to CVI tip (188 droplets). Droplets were launched at the upstream inlet with velocity equal to the free-stream velocity in a regular grid pattern. Droplets were assumed to be of unit density, and their properties were constant during the calculation.

stagnation plane for model B is found to be at $z = 0.0285$ m, which is also within the range predicted by simple theory (between $z = 0.0267$ m and $z = 0.0287$ m). (Table 1)

The predicted stagnation plane locations are both well within the range of possible values calculated from simple geometrical principles. The simple calculation is unable to accurately determine the exact length of the effective porous tube that provides the counterflow airstream because of uncertainties in how much air is passed through the region of the tube between $z = 0.0017$ m and $z = 0.0046$ m that abuts the solid wall of the CVI. The models are able to assess the effective flow through this region of the porous tube and predict the stagnation plane with greater accuracy because they include the actual measured porosity of the tube. Our results imply that relatively little flow passes through the portion of the porous tube abutting the solid region.

The numerical flow models predict the stagnation plane location to within the range of values expected by simple CVI theory, so it is reasonable to use them to calculate impaction efficiency. Because a detailed CVI flow field has been calculated, droplet trajectories can be determined without recourse to assumptions about the influence of the flow field at the CVI tip. By calculating droplet trajectories for diameter droplets, an

assessment can be made of the cut sizes for the two flow configurations.

DROPLET TRAJECTORIES

Once the velocity solutions for the different flow configurations were determined, the Lagrangian equations of motion were used to solve for the trajectories of different-sized droplets through the model. Sets of 188 unit-density droplets of each size, ranging between 10 and 500 μm in diameter for the 1 lmin^{-1} counterflow model and between 11 and 500 μm for the 3 lmin^{-1} counterflow model, were launched at the $z = -0.1$ m plane of the model over an area equal to the cross-sectional area of the CVI tip ($A = (\pi(0.0031)^2)/(2)$). The droplets were arranged in an even grid to simulate a uniform droplet concentration (Fig. 5), and their initial velocities were set equal to the free airstream (110 m/s).

When a droplet intersected the boundary of the model, its ending position was recorded, and separate code analyzed the end positions of the droplets. To calculate impaction efficiency it is only required to know if the given droplet passed through the stagnation plane. Droplets lost to the walls between the stagnation plane and the exit of the CVI (toward the sampling instruments) determine the CVI front-end transport efficiency. Any such droplets impacting on the

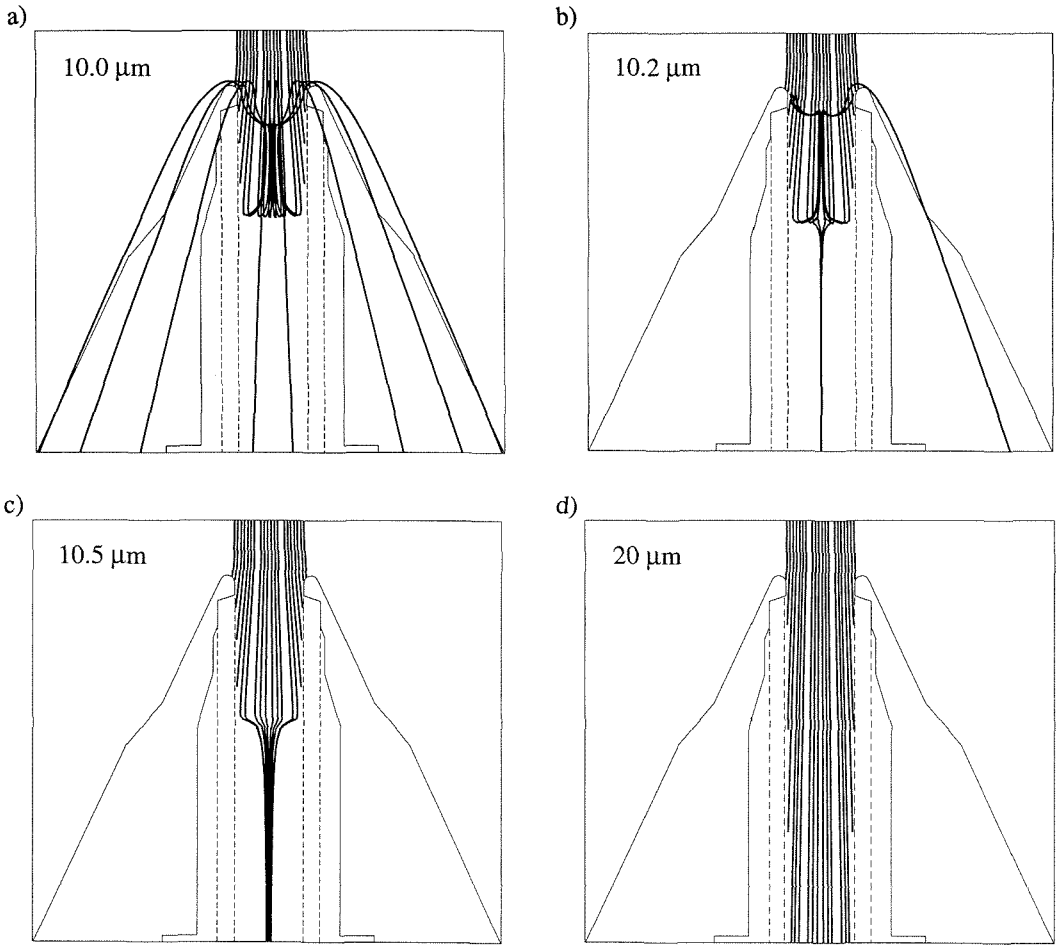


FIGURE 6. Droplet trajectories as a function of launch position for model A (1 lmin^{-1}): Droplets launched from range of initial positions at four diameters (a) $10.0 \mu\text{m}$, (b) $10.2 \mu\text{m}$, (c) $12 \mu\text{m}$, and (d) $20 \mu\text{m}$. The smallest diameter droplets follow the streamlines around the outside of the CVI. Slightly larger diameters enter the tip region, but are rejected, while droplets slightly above the cut size are collimated. Larger droplets pass the stagnation plane but have small radial (toward the wall) velocity components. (Trajectories that appear to intersect the CVI tip are actually not in the plane of the cross-section shown.)

walls of the CVI were assumed to stick to the walls and not continue in the flow. The droplets also were assumed to have constant properties (no mass loss, no heat transfer, and $\rho = 1000 \text{ kg/m}^3$).

In Fig. 6, trajectories of droplets from a range of initial positions in model A are shown. $10 \mu\text{m}$ diameter droplets have enough inertia to nearly reach, but not penetrate, the stagnation plane, S_2 . Droplets near the centerline stop just short of S_2 and

then follow the counterflow streamlines back out the CVI tip. Droplets farther from the centerline have enough outward momentum from the air flowing around the CVI tip that they impact on the inside surface of the porous tube before reaching the stagnation plane.

Slightly larger droplets ($10.2 \mu\text{m}$) pass the stagnation plane only when launched from a position on the CVI axis. Droplets launched from other positions impact on the porous tube or are turned around by the counterflow.

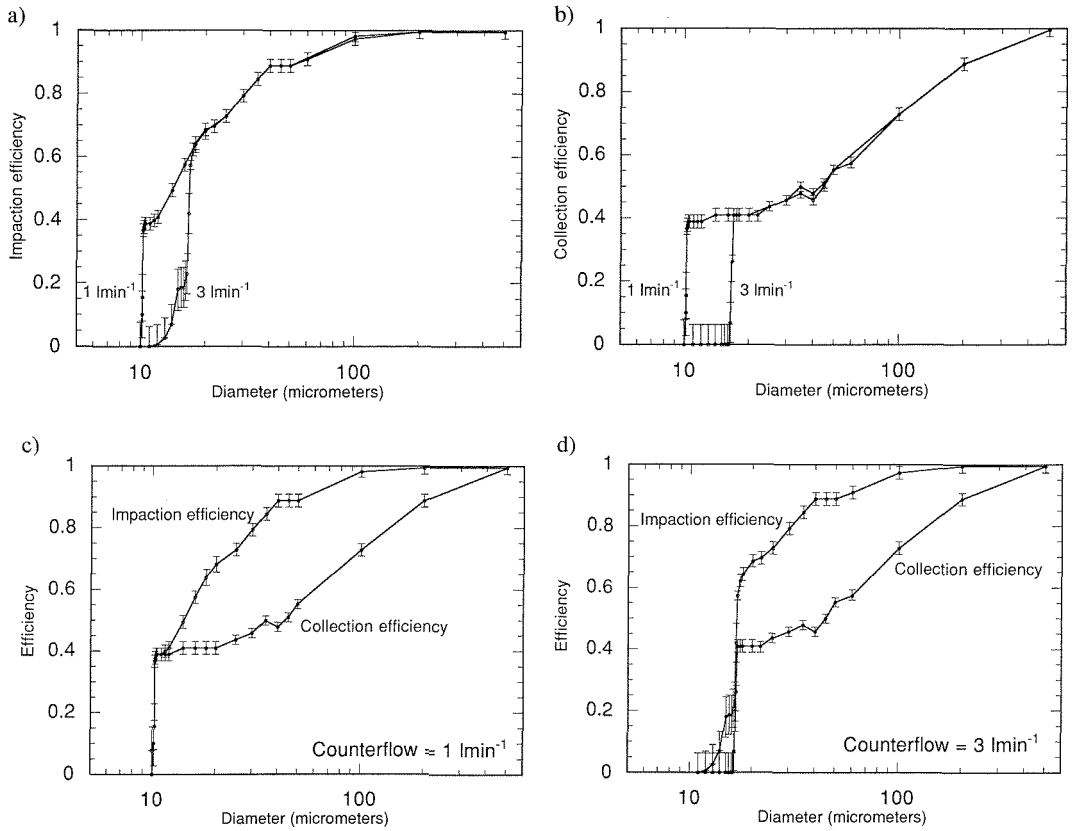


FIGURE 7. Impaction and collection efficiencies versus droplet diameter. Error bars indicate droplets trajectory uncertainties and discretization errors. Panels (a) and (b) compare each efficiency at two counterflow rates, while panels (c) and (d) compare impaction and collection efficiency at one counterflow rate (a) Impaction efficiencies for $F3 = 1 \text{ lmin}^{-1}$ and 3 lmin^{-1} , (b) Collection efficiencies for $F3 = 1 \text{ lmin}^{-1}$ and 3 lmin^{-1} , (c) Impaction and collection efficiency at $F3 = 1.0 \text{ lmin}^{-1}$, and (d) at $F3 = 3 \text{ lmin}^{-1}$.

Slightly larger diameter droplets ($10.5 \mu\text{m}$ to $\sim 12 \mu\text{m}$) that pass the stagnation plane are collimated toward the center of the CVI as a result of the inward radial velocity imparted by the flow through the porous tube. These droplets have small enough inertia so that they are still influenced by the relatively small flow through the porous tube. Larger droplets have enough inertia so that they pass the stagnation plane without significant change in direction. $20 \mu\text{m}$ droplets, for example, pass the stagnation plane with subsequent loss of droplets near the inner walls. This deposition is the result of a slight outward velocity component imparted to the droplets earlier by the flow field in the tip region (Fig. 4). The collimation

of droplets whose diameters are just large enough to pass the stagnation plane was also reported by Lin and Heintzenberg (1995). In that study the small droplets that are turned around at S_2 have similar trajectories to those shown for 10.0 and $10.2 \mu\text{m}$ in Fig. 6.

IMPACTION AND COLLECTION EFFICIENCIES FROM DROPLET TRAJECTORIES

In a CVI, the total collection efficiency for a given droplet diameter is determined by the multiplication of two terms: impaction efficiency and transport efficiency. In addition, due to the sub-isokinetic flow of the CVI, the

number concentration of droplets in the sample stream is enhanced relative to that outside the CVI. For droplets large enough to pass the stagnation plane, this enhancement factor is equal to the ratio of U_o/U , where U_o and U are the outside airspeed and the sample speed inside the CVI, respectively. When comparing data with model predictions this concentration enhancement factor is important, but for simplicity it will not be included in the discussion of impaction or transport efficiency below.

Impaction efficiency (at one droplet diameter) for the CVI model discussed above is defined as the total number of droplets (of a given diameter) that pass the stagnation plane divided by the number of droplets launched initially. Under constant ambient conditions of flow speed, temperature and pressure, impaction efficiency is simply a function of the size of the droplet and flow configuration near the tip of the CVI. Calculated impaction efficiency as a function of droplet diameter is plotted for both 1 lmin^{-1} and 3 lmin^{-1} counterflows in Fig. 7a. For both flows, impaction efficiency rises steeply at some critical diameter, and then rises more slowly, until at about $100 \mu\text{m}$ it reaches 1.0. Impaction efficiency is less dependent on counterflow rate at diameters above $20 \mu\text{m}$ than at smaller diameters.

One interesting difference between the impaction efficiency curves of the two flow configurations is the sharpness of the curve at the critical diameter. For 3 lmin^{-1} counterflow, the impaction efficiency curve does not rise steeply from zero as it does for 1 lmin^{-1} . There is a small probability that droplets with smaller diameters than the critical diameter will pass through the stagnation plane. This may be because droplets in the 3 lmin^{-1} counterflow have a longer distance over which to be collimated by the radial flow from the porous tube than those in the 1 lmin^{-1} counterflow. Droplets that normally would be turned around by the counterflow and flow out the tip instead are pushed to the centerline and have a finite probability of passing through the stagnation plane. In addition, the efficiency for 1 lmin^{-1} counterflow does not rise to 50% until the

droplet diameter is $14 \mu\text{m}$, while the efficiency of the 3 lmin^{-1} case is 50% for $17 \mu\text{m}$ droplets. Put another way, efficiencies are higher for 3 lmin^{-1} flow-field droplets near the critical diameter than for 1 lmin^{-1} , again possibly due to the increased collimation effect for the 3 lmin^{-1} counterflow. The region of the 1 lmin^{-1} efficiency curve just above the critical diameter rises less steeply than the same region above the critical diameter for 3 lmin^{-1} counterflow. This is also due to the relative importance of the collimation effect for the two counterflows.

A complete definition of transport efficiency for the CVI would be the number of droplets (of a given diameter) that travel all the way to the sampling instruments divided by the number of droplets that pass through the stagnation plane. However, because of computational limitations, the CVI flow model did not include the tube with a 90° bend that brings the droplet-laden air from the CVI front end to the sampling instruments. Therefore, for the purposes of the present CVI models, transport efficiency is defined as the number of droplets that arrive at the end of the model ($z = 0.2 \text{ m}$ plane, $r < 0.0046 \text{ m}$) compared with the number that pass through the stagnation plane.

The overall collection efficiency for the CVI front-end model is the impaction efficiency times the transport efficiency, or just the total number of droplets of a given size that arrive at the $z = 0.2 \text{ m}$ plane compared with the number launched initially. For reasons that will be discussed in "Droplet Evaporation", this collection efficiency will be a lower bound on the true CVI collection efficiency. Calculated collection efficiency curves are plotted in Fig. 7b for 1 and 3 lmin^{-1} counterflow. The curves are similar for the two cases and can be compared to the "direct" collection efficiency curves calculated by Lin and Heintzenberg (1995). In that model droplets were allowed to bounce, so "direct" collection efficiency is determined by counting only the droplets that are collected without hitting any walls. The results of the present model show the collection efficiency rising steeply at the critical diameter to 40% and then continuing to rise

less steeply for droplet diameters between the critical diameter and nearly $500\ \mu\text{m}$; the value at the knee appears to be independent of both critical diameter and CVI geometry. In comparison, the efficiency rises much more steeply after the critical diameter in the Lin and Heintzenberg model. In spite of geometrical differences, both model results show a knee at 40% efficiency. It is not understood what causes the difference in steepness above the critical diameter between the "direct" collection efficiency of Lin and Heintzenberg's model and the collection efficiency predicted by the present model, but inlet tip wall thickness and geometry differences are possible explanations.

Figures 7c and 7d compare impaction and collection efficiency for $1\ \text{min}^{-1}$ and $3\ \text{min}^{-1}$ counterflow cases, respectively. Both curves fall off steeply at the critical diameters, but the collection efficiencies remain much lower than the impaction efficiencies for droplet diameters between 10 and $500\ \mu\text{m}$. For droplets larger than $500\ \mu\text{m}$ both efficiencies are equal to 1.0. (In actuality, droplets larger than $100\ \mu\text{m}$ are expected to be removed from the airstream, either through impaction at the 90° bend or by gravitational settling, processes not included here.) The difference in the two curves for intermediate droplet diameters is a measure of transport losses between the stagnation plane and the end of the CVI model. It should be remembered that the droplets are assumed to stick to the walls. If instead the droplets were allowed to bounce and be re-entrained in the sample flow, the collection efficiency would be much higher and equal to the impaction efficiency. Whether the droplets actually bounce (e.g., Lin and Heintzenberg, 1995) or stick is not known, but this question is further addressed in relation to actual data (see "Discussion").

Figure 8 shows the mechanism for loss of droplets between the cut size and $200\ \mu\text{m}$ in diameter. Trajectories are shown for four droplets of different diameters launched from the same position near the edge of the inlet (the least favorable initial position). Droplets of all sizes are pushed radially outward at the tip, and those droplets closest to

the CVI wall will be deposited before they can travel the length of the inlet. Smaller droplets (such as the 10 and $20\ \mu\text{m}$ drops in Fig. 8a and b) with less inertia will be deposited closer to the tip, often in front of the stagnation plane, because they are most influenced by the streamlines. Droplets of intermediate diameter will be less influenced by the radial tip field and therefore will pass through the stagnation plane but still be deposited somewhere along the wall before the end of the model ($50\ \mu\text{m}$ in Fig. 8c). Only the largest droplets (e.g., $200\ \mu\text{m}$) near the inner walls will pass through the end of the inlet. Droplets of intermediate diameters near the inner wall of the CVI that have enough inertia to pass the stagnation plane therefore will have the largest transport losses. This mechanism accounts for the flatness of the collection efficiency curves between the cut size and $\sim 50\ \mu\text{m}$. In general, droplets launched along the CVI centerline will have a greater chance of being collected.

CVI Cut Size

According to simple aerodynamic considerations (Fuchs, 1964), a particle's stopping distance (distance traveled in quiescent air) must exceed the distance the particle has to travel from the tip to the flow separation point, L_{cvi} , in order to be collected. L_{cvi} is the sum L_{por} plus L_{tip} as indicated in Fig. 1. The minimum particle size that is collected by the probe can be selected by adjusting the $F3/F1$ ratio and therefore the distance, L_{por} ($L_{por} = (F3/F1)X$, where X is the total length of the porous tube.) As L_{cvi} increases, so does the size of particle that can be collected; this allows different diameter particles to be collected so that their properties can be compared. The particle stopping distance, \mathcal{L} , can be described as

$$\mathcal{L} = Vm_p Bf,$$

where V is the free airstream velocity, m_p is particle mass, and B is particle mobility ($= (1/6\pi\mu r_p)$, μ being the air viscosity and r_p the particle radius). f , a function of the particle Reynolds number, is a correction

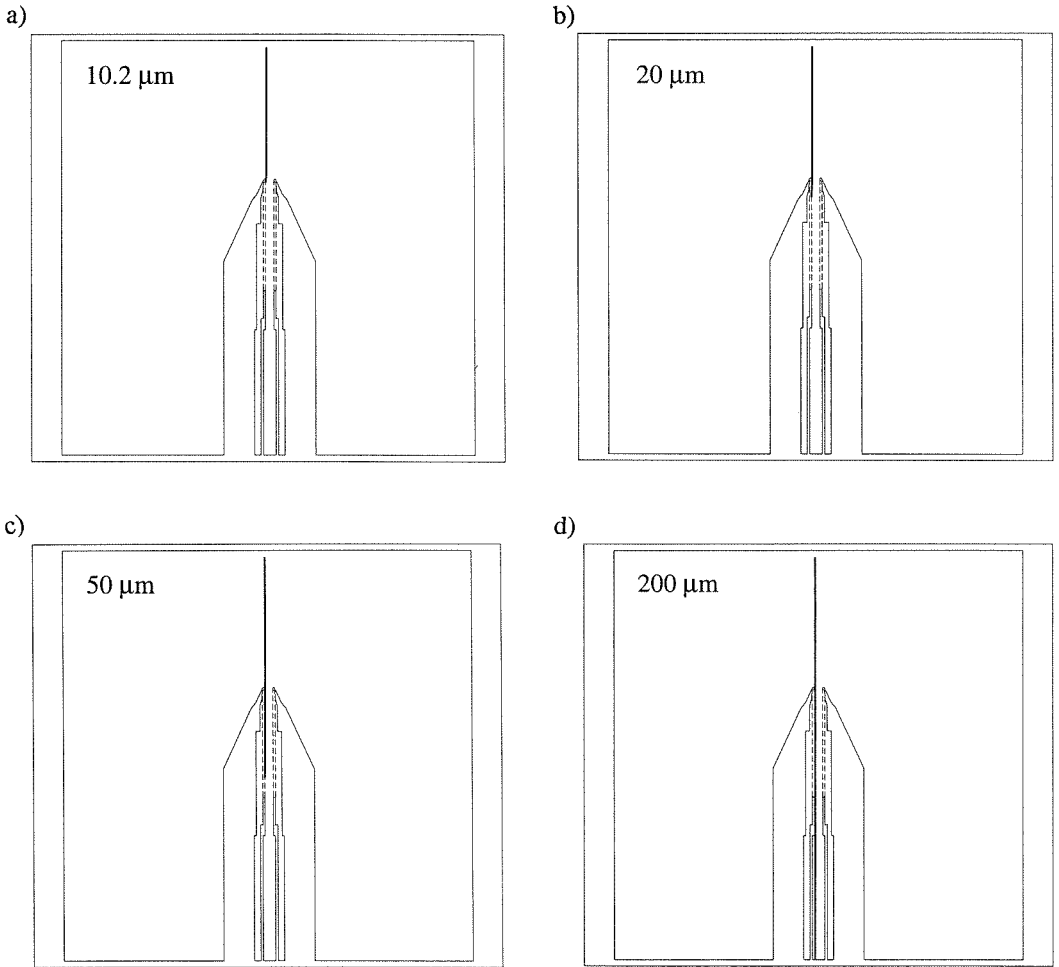


FIGURE 8. Trajectories of droplets launched near the CVI walls, as a function of diameter. Droplets are launched from the same initial position (near the wall) for four diameters: (a) 10.2 μm , (b) 20 μm , (c) 50 μm , and (d) 200 μm . The smaller diameter droplets impact the wall near the tip, while the larger diameter droplets pass through the stagnation plane and impact the wall closer to the end of the inlet. The 200 μm droplets are collected.

factor for non-linear drag effects (Serafini, 1954) given by,

$$f = \frac{3}{Re_p \kappa^{3/2}} \left[Re_p^{1/3} \kappa^{1/2} + \arctan(Re_p^{-1/3} \kappa^{-1/2}) - \frac{\pi}{2} \right],$$

where $Re_p = \rho_p DV / \mu$ is the particle Reynolds number and κ is a constant equal to 0.158 (Noone et al., 1988b).

Cut size, or critical diameter, for a CVI has been estimated before (Noone et al., 1988a) by assuming that for a given flow configuration the droplet stop distance, \mathcal{L} , must fall between L_{cvi} and $L_{cvi} + 1.6R$ (Anderson et al., 1993), where L_{cvi} is the distance from stagnation plane to tip and R is the outer radius of the tip ($R = 0.0046$ m in this case). CVI cut sizes have been calibrated (Noone et al., 1988b; Anderson et al., 1993) and found generally to agree with this simple impaction theory (Fuchs, 1964).

For a counterflow of 1 lmin^{-1} , the distance between the stagnation plane and the tip was found (with the numerical model) to be 0.0123 m. Therefore, the stop distance corresponding to the cut size would be predicted to lie between 0.0123 m (L_{cvi}) and 0.0197 m ($L_{cvi} + 1.6R$). This corresponds to an expected cut size (calculating successive approximations where $T = 50^\circ\text{C}$, $P = 900 \text{ mb}$) of between $9.25 \mu\text{m}$ and $12.3 \mu\text{m}$. For 3 lmin^{-1} counterflow, the distance between the stagnation plane and the CVI tip was 0.0285 m, so the stop distance of the droplet that just passes the stagnation plane would be predicted to lie between 0.0285 m and 0.0358 m, and the expected cut size would be between $15.4 \mu\text{m}$ and $18.5 \mu\text{m}$.

The cut sizes determined by the CVI flow model can be read off the impaction efficiency curves (Figs. 7c and 7d). The curves for 1 lmin^{-1} counterflow show a very steep rise from 0 to 40% efficiency between 10 and $12 \mu\text{m}$, 90% of this rise occurring between 10 and $10.25 \mu\text{m}$. The same curves for 3 lmin^{-1} counterflow show a similarly steep rise between $16 \mu\text{m}$ and $18 \mu\text{m}$. Previous impaction efficiency curves from experimental calibrations are not as sharp, so that cut sizes were given as the size at which the efficiency was 50%. For numerical modeling results, we use a working definition of the cut size as the midpoint of the droplet diameter range where the impaction efficiency more than doubles within a $1 \mu\text{m}$ interval. With this definition, the cut size for 1 lmin^{-1} counterflow is $10.1 \mu\text{m}$, and for 3 lmin^{-1} counterflow it is $17.0 \mu\text{m}$. These values fall well within the range of cut sizes calculated from the simple theory above. The stop distance for a $10.1 \mu\text{m}$ droplet is 0.0133 m and for a $17 \mu\text{m}$ droplet it is 0.0312 m. These distances can be expressed as $L_{cvi} + 0.3R$ and $L_{cvi} + 0.9R$ for the two counterflow cases, respectively.

Droplet Evaporation

The flow models did not include the evaporation of droplets that may occur during impaction and transit of the CVI front end. This simplification was based on results of a

one-dimensional heat and mass transfer model (Anderson, 1992; Pruppacher and Klett, 1978) used to estimate the potential importance of evaporation within the CVI front end. The details of this model can be found in the Appendix. To summarize, droplet evaporation is not significant upstream of the stagnation plane but may affect the droplet trajectories between the stagnation plane and the end of the flow model. As a larger droplet (above the cut size) moves into the region downstream of the stagnation plane, it begins to evaporate, and as it does so, it slows down to a velocity approaching that of the sample stream flow. As the droplet diminishes in size, it more closely follows the sample flow streamlines, and so has a reduced probability of impacting the walls. Thus, droplet evaporation is expected to increase the collection efficiency of a CVI. When evaporation is not included, the results from droplet trajectory calculation will underestimate the total collection efficiency of the CVI.

In order to fully understand the dynamics of the competing effects of diminishing inertia versus radial velocity due to tip flow, droplet equations of motion should be linked to heat and mass transfer equations. For a more complete treatment of CVI collection efficiency, evaporating droplets should be included in the numerical flow model.

Errors

Two digitization errors occur when calculating droplet impaction and collection efficiencies. Because a smooth distribution of droplets is represented by a uniform grid of droplets with a finite resolution, a quantization error (± 1 drop) results. Flow-field symmetry requires this quantization error to be mirrored across the symmetry plane, making the error $\pm 2/188$ or $\pm 1.1\%$. A second digitization error occurs because the area mapped out by the 188 droplets is not exactly the area of the CVI half-inlet ($A = \pi (0.0031^2)/(2)$); thus, a further digitization error of $188\Delta x\Delta y/A = 1.1\%$ is incurred. Both these errors are random, i.e., they can either

add or subtract from the number of droplets ending in each region.

A small number of droplets (22 out of 188) were "lost" between cells of the model due to trajectory discretization errors; in the version of the trajectory code used to calculate collection and impaction efficiencies, droplets were allowed just three steps through each cell in the model. The initial positions of some droplets were so close to the boundary between cells that three steps were not enough to get to the next cell, and the trajectory calculation stopped. This error introduces uncertainty in the number of droplets terminating in each region. Since droplets are always lost from the same initial positions, the uncertainty sometimes affects the collection efficiency and sometimes the impaction efficiency, depending on the droplet size. However, this uncertainty was only significant for small droplet sizes (near the cut size) since, for larger sizes, most of the "lost" droplet end positions could be determined from continuity with nearby droplet end positions. At large droplet sizes, only the droplets missing on the boundary of different regions contributed to the uncertainty in the number counted in the two regions (generally not more than two counts).

An indication of the minimum and maximum counts possible including all the above errors for each droplet size is indicated in Fig. 7 by error bars on the efficiency curves. However, these errors do not account for the dip in collection efficiency at 40 μm , for both counterflows. This dip is probably not physical because it occurs in the same place for both counterflow configurations.

Using a new version of the trajectory code, which allowed a user-specified number of steps per cell, trajectories for droplet diameters between 30 and 45 μm were recalculated using 10 steps per cell. It is interesting to note that there were no droplets lost in these trajectory calculations. In this region, the collection efficiency changed by, on average, -2.5 counts (out of 188, or -1%), and at the most -4 counts (-2%); the impaction efficiency changed by an average of -3.5 counts (-2%), and at most -10 counts (-5%). Although in the new calculation the

collection efficiency at 40 μm was still lower by about 2% than that at 35 μm , errors due to the finite number of steps per cell are of the right magnitude to account for such features in the collection efficiency curve. Other, at present unknown, discretization errors in the code may also contribute to the ripples in the collection efficiency curves.

Discussion

The CVI model results presented here elucidate the nature of the CVI flow field, as well as some aspects of droplet behavior within the CVI. Our results also compare favorably with previous calculations of CVI cut size and impaction efficiency. Still, the important question of how our calculations compare with real CVI instruments has not yet been considered. Laboratory calibrations conducted in the past have not completely addressed the problem of CVI collection efficiency (CE) because the calibrations have either been relative (assuming 100% collection at some reference droplet size (Noone et al., 1988b)) or have used glass beads (Anderson et al., 1993), which bounce on impact with the walls and therefore may not be representative of wet droplets. CVI collection efficiency can also be studied by comparing it with that of other instruments during field experiments. Here we discuss some field measurements and compare them with model results.

In marine stratus clouds, the number of residual particles collected by the CVI was compared with the number of droplets measured with the forward-scattering spectrometer probe (FSSP-100) above the CVI cut size (Twohy, 1992). This comparison yielded a CVI CE (relative to the FSSP) of about 0.5, and subsequent comparisons in other airborne experiments yield similar CE values. Twohy (1992) also showed that residual particle mass collected behind the CVI after droplet evaporation yielded only about half of the solute mass collected by a slotted-rod sampler, in which droplets are impacted on rods and collected as a bulk liquid sample. Condensed water content inferred from the CVI water vapor measurements (made with

a Lyman- α hygrometer), however, tends to agree favorably with both the FSSP and the more accurate hot-wire probe (Twohy et al., 1997). This suggests that some droplets impact and stick on the CVI walls, then evaporate, so that the water vapor associated with these droplets is transmitted downstream, while their residual nuclei adhere to the walls.

Although collection efficiency is size-dependent and therefore dependent on the droplet size distribution, we can make a first-order comparison of these field results with our model results by averaging our calculated impaction and collection efficiency values for sizes between the cut size and 50 μm diameter, where most of the number density is concentrated in a cloud. Using this method for model A, the overall impaction efficiency is about 0.73, while CE (which assumes that droplets stick when they contact a wall downstream of the stagnation plane) is only about 0.45. These numbers agree favorably with the experimental CEs of 0.5. However, the situation is complicated by processes not included in the model, as discussed below.

First, evaporation is not included in the model. Due to the tendency of evaporating (smaller) droplets to more closely follow flow streamlines, evaporation is expected to increase predicted collection efficiency, while having a negligible effect on impaction efficiency. Thus with evaporation, we expect overall collection efficiency to be somewhat higher than 0.45, with a maximum equal to the overall impaction efficiency of 0.73. Second, the model predicts CVI particle CE to be relatively insensitive to cut size (Fig. 7b), and we do not expect evaporation to change this trend. However, CE is observed to decrease at larger cut sizes (Twohy, 1992, as well as unpublished data). Also, a strong dependence of collection efficiency on aircraft attack angle was observed. Twohy (1992) postulated that the lower CE of large droplets might result from impaction on CVI inlet walls if droplet trajectories were not initially aligned with the longitudinal axis of the CVI tip. (This process is similar but independent of the deposition due to the

radially outward flow at the CVI tip discussed earlier in "Impaction and Collection Efficiencies from Droplet Trajectories"). These losses could occur if the CVI inlet was misaligned, even by one or two degrees, with airflow streamlines around the aircraft. Collection efficiencies near 100% achieved with the ground-based CVI (Hallberg et al., 1994; Lin and Noone, 1996) might be explained by better alignment of that CVI, which is contained in a flow-collimating wind tunnel, by enhancements in droplet concentration that may occur in the wind tunnel upstream of the CVI inlet (Noone et al., 1992), or by other differences in probe geometry and experimental conditions.

One other process that affects actual collection efficiency is not included in the model, namely deposition in the 90° bend downstream of the inlet. This is also expected to decrease CE for larger droplets; however, calculations indicate this loss mechanism is not very important for droplets smaller than about 50 μm diameter. (The actual size depends on the actual internal configuration of the CVI bend.) Thus, a minimal effect on particle number concentration is expected.

To summarize, collection efficiencies determined from field experiment are consistent with those calculated in this work. However, two important processes are not included in the model: namely, droplet evaporation (which will increase CE) and losses due to misalignment of the CVI tip with the oncoming airflow (which will decrease CE). These competing processes may fortuitously contribute to the agreement between theory and experiment. To determine collection efficiency more accurately, we should include evaporation in the model and strive to eliminate losses due to misalignment of the CVI tip.

Droplet trajectories can be aligned upstream of the airborne CVI by incorporating a shroud around the CVI tip, as described in another paper (Twohy, 1997). Results from flight tests of the shrouded CVI will be used to determine whether collection efficiency improves substantially when trajectories are initially aligned with the CVI axis. Collection

efficiency could be further enhanced by modifying the inlet to segregate and utilize only particles from the center of the CVI sample stream. Another possibility would be to utilize a converging shroud to direct droplets radially inward, and thereby counteract the effects of the outward flow at the CVI tip.

CONCLUSIONS

Numerical flow models of a CVI operating at 900 mb (ambient pressure) with 1 and 3 lmin^{-1} counterflow were constructed in order to calculate impaction and front-end collection efficiency as functions of droplet diameter. Several important results emerged:

1. The flow model predicted locations of the stagnation planes for the two flow configurations within the ranges calculated by simple geometrical considerations.
2. Cut sizes predicted from the efficiency curves ($10.1 \mu\text{m}$ for 1lmin^{-1} counterflow and $17.0 \mu\text{m}$ for 3lmin^{-1}) agree well with cut size ranges calculated previously (Anderson et al., 1993) and allow us to fine-tune the simple parameterization of cut size for this particular CVI.
3. The above results indicate that the numerical code (STAR-CD) is adequate for the complex flow field analyzed in this study.
4. The collection efficiency results for water droplets from these flow models show that there may be significant losses between the stagnation plane and the exit of the CVI front end for diameters between 12 and $500 \mu\text{m}$; these losses are due to an outward velocity component imparted to the droplets just upstream of the CVI tip.
5. Cut sharpness as determined from the numerical flow models is much higher than that determined by experiment (Anderson et al., 1993) but agrees with Lin's two-dimensional numerical potential flow model (Lin and Heintzenberg, 1995). The cause of this is unknown but is probably related to experimental non-idealities.
6. Impaction efficiency for diameters be-

tween the cut size and about five times the cut size is lower than that calculated by Lin and that reported by Anderson for dry glass beads because the present study assumes that droplets stick to the walls on impaction.

7. Impaction efficiency at the cut size increases with increasing counterflow (as the stagnation plane moves farther away from the tip).
8. Because transport between the CVI front end and the sampling instruments is slow enough for substantial evaporation to occur, our calculations represent a lower limit on transport efficiency. A more complete analysis of CVI collection efficiency must include heat transfer and exchange of mass and heat with the droplets.
9. Calculated collection efficiencies are in general agreement with results from CVI field measurements. However, more accurate results could be obtained by the model if the effects of droplet evaporation were included, and if a flow straightening shroud were added to the actual CVI to assure proper alignment of the impinging droplets.

APPENDIX: ONE-DIMENSIONAL MODEL FOR DROPLET EVAPORATION

In this appendix, a one-dimensional heat and mass transfer model (Anderson, 1992; Pruppacher, 1978) is used to estimate the effects of droplet evaporation on the trajectory results discussed in the body of the paper. In this model, droplets are assumed to move into a region of stagnant, dry air (vapor pressure and velocity of stagnant air are zero) and the droplet remains isothermal. Ventilation factors are used to estimate the increased transfer rates of heat and mass due to the large droplet velocities relative to air.

Results from this heat and mass transfer model indicate that the ratio of evaporation time, τ_{evap} , to stopping time, τ_{stop} , is large for all droplet sizes between 4 and $100 \mu\text{m}$. τ_{evap} is defined to be the time a droplet takes

to evaporate completely and τ_{stop} is the model-calculated time required for the droplet to slow to 0.1 of its original speed (τ_{stop} is larger, and therefore more conservative for this comparison than the characteristic relaxation time for Stokes flow, τ_{relax} , which is defined as the time required to slow to $1/e$ of the droplet's initial speed). The ratio τ_{evap}/τ_{stop} depends on the droplet size as well as the air temperature in the CVI; for 50°C, it ranges from 129 for 4 μm drops to 615 for 100 μm drops. These results imply that there is no significant evaporation upstream of the stagnation plane for any droplet size. Therefore, there will be no significant error introduced by ignoring droplet evaporation in calculating CVI impaction efficiency.

However, the calculation of transport efficiency between the stagnation plane and the $z = 0.2$ m plane is complicated by the fact that the time it takes droplets to pass from the stagnation plane to the sampling instruments is long enough for substantial droplet evaporation to occur at all diameters. Droplet evaporation depends on the temperature, relative humidity, and flow field in the CVI and with high enough droplet concentrations, the presence of other droplets. The change in droplet size as a function of time can be calculated using Maxwell's equation (Pruppacher, 1978), which when integrated gives:

$$D(t) = D(0) \sqrt{1 - \frac{t}{\tau_{evap}}},$$

where $D(0)$ is the initial droplet diameter and

$$\tau_{evap} = \frac{D(0)^2 \rho R T}{8 M_w D_v (e_s(T) - e_{inf})}.$$

ρ is the droplet density, R is the gas constant ($8.31 \times 10^7 \text{ erg/mole-K}$), T is the droplet temperature, which is assumed to remain constant during evaporation, M_w is the molecular weight of water, D_v is the diffusivity of water vapor in air, $e_s(T)$ is the saturation vapor pressure at temperature T , and e_{inf} is the water vapor pressure in the ambient air.

τ_{evap} is the time required for a droplet of a given diameter to evaporate completely in the approximation that at all times during evaporation the droplet remains at a constant temperature (i.e., the cooling due to latent heat loss is always exactly balanced by the heating due to conduction from the air).

In the region between the stagnation plane and the end of the flow model ($z = 0.2$ m), smaller droplets move with the velocity near that of the sample stream, while larger droplets will move at higher velocities. An upper bound on the droplet size that will completely evaporate during its transit between the stagnation plane and the end of the model can be determined by assuming the droplet moves at the sample stream velocity. The droplet transit time will be 0.09 and 0.11 seconds for 1 lmin^{-1} and 3 lmin^{-1} counterflow models, respectively. In this time, droplets with diameters below 17 μm for 1 lmin^{-1} flow and below 19 μm for 3 lmin^{-1} flow will evaporate completely. Thus we can expect that evaporation is important for droplets after they pass the stagnation plane.

Because of the large inertia changes in an evaporating droplet, trajectories of such droplets will be very different from those of constant mass droplets. Droplets shrinking downstream of the stagnation plane will be more likely to follow the streamlines as they move with the sample stream and thus will have a higher probability of passing the $z = 0.2$ m plane without impacting on the walls. Therefore, results from the droplet trajectory calculations will underestimate the number of droplets of all sizes collected at the downstream end of the CVI model and thus will underestimate the total collection efficiency of the CVI.

We would like to thank Tad Anderson for reading and discussing a preliminary version of this paper and Robert Charlson for his support of this work. This work was partially supported by NASA's Aerosol Interdisciplinary Research Program (W-18451), its Atmospheric Effects of Aviation Project (A-45563D), and the National Science Foundation (Grant ATM-9320871).

References

- Anderson, T. L. (1992). Optimization of a Counterflow Virtual Impactor (CVI) for Studying Aerosol Effects on Cloud Droplet Number. Ph.D. dissertation, Department of Atmospheric Sciences, University of Washington, Seattle, WA.
- Anderson, T. L., Charlson, R. J., and Covert, D. S. (1993). Calibration of a Counterflow Virtual Impactor at Aerodynamic Diameters from 1 to 15 μm , *Aerosol Sci. Technol.* 19:317-329.
- Baumgardner, B., Huebert, B. and Wilson, C. (1990). Meeting review: Airborne aerosol inlet workshop, NCAR Technical Note NCAR/TN 362 + 1A, National Center for Atmospheric Research, Boulder, CO.
- Fuchs, N. A. (1964). *The Mechanics of Aerosols*, Dover Publications, New York.
- Hallberg, A., Noone, K. J., Ogren, J. A., Svenningsson, I. B., Flossman, A., Weidensohler, A., Hansson, H.-C., Heintzenberg, J., Anderson, T. L., Arends, B., and Maser, R. (1994). Phase Partitioning of Aerosol Particles in Clouds at Kleiner Feldberg, *J. Atmos. Chem.* 19:107-207.
- Huebert, B. J., Lee, G., and Warren, W. L. (1990). Airborne Aerosol Inlet Passing Efficiency Measurement, *J. Geophys. Res.* 95: 16,369-16,381.
- Lauder, B. E., and Spalding, D. B. (1974). Numerical Computation of Turbulent Flows, *Computer Methods in Applied Mechanics and Engineering* 3:269-289.
- Lin, H., and Heintzenberg, J. (1995). A theoretical study of the Counterflow Virtual Impactor. *J. Aerosol Sci.* 26:903-914.
- Lin, H., and Noone, K. J. (1996). A Simulation of Cloud Formation and Sampling Using the Counterflow Virtual Impactor, *Beitr. Phys. Atmosph.* 69(2):321-332.
- Noone, K. J., Charlson, R. J., Covert, D. S., Ogren, J. A. and Heintzenberg, J. (1988a). Cloud Droplets: Solute Concentration Is Size Dependent, *J. Geophys. Res.* 93D:9477-9482.
- Noone, K. J., Ogren, J. A., Heintzenberg, J., Charlson, R. J. and Covert, D. S. (1988b). Design and Calibration of a Counterflow Virtual Impactor for Sampling of Atmospheric Fog and Cloud Droplets, *Aerosol Sci. Technol.* 8:235-244.
- Noone, K. J., Ogren, J. A., Noone, K. B., Hallberg, A., Fuzzi, S., and Lind, J. A. (1991). Measurements of the Partitioning of Hydrogen Peroxide in a Stratiform Cloud, *Tellus* 43B: 280-290.
- Noone, K. J., Hansson, H.-C., and Mallant, R. K. A. M. (1992). Droplet Sampling from Crosswinds: An Inlet Efficiency Calibration, *J. Aer. Sci.* 23:153-164.
- Noone, K. B., Noone, K. J., Heintzenberg, J., Strom, J., and Ogren, J. A. (1993). In Situ Observations of Cirrus Cloud Microphysical Properties Using the Counterflow Virtual Impactor, *J. Atmos. Oceanic. Technol.* 10:294-303.
- Ogren, J. A., Heintzenberg, J., and Charlson, R. J. (1985). In Situ Sampling of Clouds with a Droplet to Aerosol Converter, *Geophys. Res. Lett.* 12:121-124.
- Ogren, J. A., Heintzenberg, J., Zuber, A., Noone, K. J., and Charlson, R. J. (1989). Measurements of the Size-Dependence of Solute Concentrations in Cloud Droplets, *Tellus* 41B:24-31.
- Ogren, J. A., Noone, K. J., Hallberg, A., Heintzenberg, J., Schell, D., Berner, A., Solly, I., Krusiz, C., Reischl, G., Arends, B. G., and Wobrock, W. (1992). Measurements of the Size Dependence of the concentration of Non-volatile Material in Fog Droplets, *Tellus* 44B:570-580.
- Patankar, S. V. (1980). *Numerical Heat Transfer and Fluid Flow*, Hemisphere Publishing, New York.
- Patankar, S. V., and Spalding, D. B. (1972). A Calculation Procedure for Heat, Mass and Momentum Transfer in Three-dimensional Parabolic Flows. *Int. J. Heat Mass Transfer* 15:1787-1806.
- Pruppacher, H. R., and Klett, J. D., (1978). *Microphysics of Clouds and Precipitation*, D. Reidel Publishing Co., Dordrecht, Holland.
- Serafini, J. S. (1954). Nat. Adv. Comm. Aeron., Report 1159, Impingement of Water Droplets on Wedges and Double-wedge Airfoils at Supersonic Speeds (1960). NACA Report #1159, 40th Annual Report of the National Advisory Committee for Aeronautics, 1954. U.S. G.P.O. Washington, D.C. pp. 85-108.
- Strom, J., Heintzenberg, J., Noone, K. J., Noone, K. B., Ogren, J. A., Albers, F., and Quante, M. (1994). Small Crystals in Cirriform Clouds: A Case Study of Residue Size Distribution, Cloud Water Content, and Related Cloud Properties, *Atmos. Res.* 32:125-141.
- Twohy, C. H., Clarke, A. D., Warren, S. G., Radke, L. F., and Charlson, R. J. (1989). Light

- Absorbing Material Extracted from Cloud Droplets and Its Effect on Cloud Albedo, *J. Geophys. Res.* 94:8623–8631.
- Twohy, C. H. (1992). On the Size Dependence of the Chemical Properties of Cloud Droplets: Exploratory Studies by Aircraft, Ph.D. dissertation, NCAR Cooperative thesis CT-137, Department of Atmospheric Sciences, University of Washington, Seattle, WA.
- Twohy, C. H., and Rogers, D. (1993). Airflow and Water-Drop Trajectories at Instrument Sampling Points around the Beechcraft King Air and Lockheed Electra, *J. Atmos. Oceanic. Technol.* 10:566–578.
- Twohy, C. H., Schanot, A. J., and W. A. Cooper (1997). Measurement of Condensed Water Content in Liquid and Ice Clouds Using an Airborne Counterflow Virtual Impactor, *J. Atmos. Ocean. Tech.* 14:197–202.
- Yakhot, V., Orszag, S. A., Thangam, S., Gatski, T. B., and Speziale, C. G. (1992). Development of Turbulence Models for Shear Flows by a Double Expansion Technique, *Phys. Fluids* 4(7):1510–1520.
- Received 25 February 1997, accepted 18 August 1997.